From Faces To Volumes - Measuring Volumetric Asymmetry in 3D Facial Palsy Scans[★]

Tim Büchner[1][0000−0002−6879−552X], Sven Sickert[1][0000−0002−7795−3905], Gerd Fabian Volk[2][0000−0003−1245−6331], Orlando Guntinas-Lichius[2][0000−0001−9671−0784], and Joachim Denzler[1][0000−0002−3193−3300]

[1] Computer Vision Group, Friedrich Schiller University Jena, 07743 Jena, Germany
{tim.buechner,sven.sickert,joachim.denzler}@uni-jena.de
[2] Dept. of Otorhinolaryngology, Jena University Hospital, 07747 Jena, Germany
{orlando.guntinas}@med.uni-jena.de

Abstract. The research of facial palsy, a unilateral palsy of the facial nerve, is a complex field of study with many different causes and symptoms. Even modern approaches to evaluate the facial palsy state rely mainly on stills and 2D videos of the face and rarely on 3D information. Many of these analysis and visualization methods require manual intervention, which is time-consuming and error-prone. Moreover, existing approaches depend on alignment algorithms or Euclidean measurements and consider only static facial expressions. Volumetric changes by muscle movement are essential for facial palsy analysis but require manual extraction. Our proposed method extracts an estimated unilateral volumetric description for dynamic expressions from 3D scans. Accurate positioning of 3D landmarks, problematic for facial palsy, is automated by adapting existing methods. Additionally, we visualize the primary areas of volumetric disparity by projecting them onto the face. Our approach substantially minimizes human intervention simplifying the clinical routine and interaction with 3D scans. The proposed pipeline can potentially more effectively analyze and monitor patient treatment progress.

Keywords: Facial Volumes · Facial Palsy · Radial Curves · Emotions

1 Introduction

Advancements in imaging techniques provide novel insights across various disciplines, particularly in the medical field. Especially in the area of facial palsy, a unilateral palsy of the facial nerve [25], 3D scans offer new capabilities to analyze the treatment progress. The limiting scope of 2D images cannot capture the full extent of the palsy, and, therefore, 3D models could bridge this gap [15,25]. Obtaining volumetric information can be an indicator for facial changes [4,21],

as facial muscle contractions, in reality, lead to 3D volume shifts of facial soft tissues, i.e., the muscle, fat tissue, and overlying skin.

Many methods for processing 3D data involve human interaction [15, 23], making them time-consuming and prone to errors. Our work aims to develop an automated method for estimating unilateral facial volumes from generated meshes. We visualize the disparities in a patient's 3D scan to guide the medical professional's decision-making process for treatment during the clinical routine. First, we provide a method to reliably place 3D facial landmarks for patients with facial palsy and reduce the runtime of exiting methods by 96.6% [18]. Next, we extract radial curves from the 3D scan, starting at the nose tip [2–4, 24]. These curves offer a detailed and structured description of the face surface for lateral comparisons. Our approach minimizes human intervention is fully automatic after parameter selection, and is available as open-source software[3].

2   Related Work

Existing methods for assessing facial palsy [9, 20, 26] rely on 2D images, either by using landmarks [12, 14] or neural networks [20] to estimate existing palsy grading. However, many critical facial features cannot be captured by 2D images, such as the depth of the face or the volume differences between the face sides. Additionally, head rotation contributes to difficulties in analyzing 2D images.

3D morphable models are a common way to describe 3D face scans [11, 13, 19]. These incorporate landmarks as the primary reference points during the fitting [11] or leverage a symmetric template model acquired from healthy faces [13,19]. However, facial palsy patients have a wide range of asymmetry during facial movements, so these methods are unsuitable for this task. The fitting process eliminates detailed information on the face surface, which we require for understanding small volume changes. Consequently, we refrain from using 3D morphable models for lateral comparisons giving up semantic knowledge for a more comprehensive description of the face surface. Current methods for tracking volume changes in the mid and lower face rely on sparse features [21]. Their findings indicate that subtle facial expressions lead to measurable volume changes, which we aim to capture using a dense representation.

Some 3D palsy assessment methods require manual interaction [15,16,22,23], while others attempt automation [4, 24] but focus only on face surface analysis. Utilizing radial curves [3,4] shows potential for detailed anatomical descriptions. Initially aligned using landmarks, the curves remain on the original face scan surface, retaining their features and overcoming template-based limitations. Radial properties enable structured face surface descriptions divided into distinct regions. Existing facial palsy approaches demonstrated this [4]. Nonetheless, the one-to-one mapping between curve points eliminates the influence of each side on the other. We overcome limitations by generating lateral face meshes using radial curves and revealing volume disparities between both facial sides.

---

[3] https://github.com/cvjena/corc

3   Data Acquisition

We investigate volumetric changes in patients with facial palsy. Facial muscle contractions lead to 3D volume shifts of facial soft tissues, i.e., the muscle, fat tissue, and overlying skin [21]. We used the 3dMD face system (3dMD LCC, Georgia, USA) to capture these movement exercises, generating a 3D facial mesh using multiple 2D images and infrared structured light. This setup ensures that the mesh faces towards the z-axis, and the face remains close to the coordinate system's center. The patients follow an instruction tutorial and are asked to maintain a neutral expression for 3 seconds, followed by 3 seconds of smiling.

We recorded patients suffering from postparalytic facial syndrome at their treatment's beginning and end. Our data contains only patients with unilateral chronic synkinetic facial palsy with symptoms persisting for over six months. A common symptom in flaccid facial palsy is muscle atrophy, the affected side has a lower volume than the healthy side [25]. Volume changes are expected due to the imbalance on the affected and the contralateral side in the synkinetic patients.

4   Methods

Our goal is to achieve a fully automatic analysis of volumetric changes caused by facial tissue shifts during muscle contractions. Furthermore, we want to visualize the local volumetric differences between the face sides. First, we extract 3D landmarks from the 3D scan by adapting existing methods to patients with facial palsy [18]. Second, we obtain radial curves from the 3D scan using these landmarks [4]. Third, we develop a volumetric description of the face sides based on the radial curves. Lastly, we employ the lateral properties of radial curves to produce a disparity heatmap and compare it to the volumetric results. Our method also applies to point clouds, as we use only the vertices of the 3D mesh.

4.1   3D Landmark Extraction for Facial Palsy Patients

The structured semantic representation of 3D facial features is crucial for many processing steps. Either by landmarks or 3D morphable models (3DMM) [11, 13, 18], these representations are the basis for further analysis. Models estimating these descriptors train on healthy faces, thus, unsuitable for patients with facial palsy and necessitate manual intervention [15, 23]. As 3DMMs modify the template surface for fitting [11], they are unsuitable for volume analysis. We opt for a multi-view consensus 3D landmark extraction method introduced by [18] and adapt it to patients with facial palsy. They use several virtual camera views ($n = 96$) around the face to estimate 2D landmarks. Utilizing the intrinsic and extrinsic camera parameters, the 2D landmarks are projected onto the 3D mesh.

We aim for a fast, automatic approach to support medical practitioners during the clinical routine. The original implementation takes 30 seconds to extract the landmarks for one single scan on an Nvidia GeForce GTX 3070 [18]. Hence, processing a six-second video (at 30 frames per second) would take around 5400

Fig. 1: Virtual camera locations to approximate 3D landmarks using [18]: The camera positions are on a sphere around the face to generate lateral views.

seconds (90 minutes). Instead of using 96 random camera locations, we achieve suitable landmarks with only eight fixed camera locations. We focus on lateral views of the face[4], depicted in Figure 1, to minimize unknown symmetry biases in the learned model. The 3D facial landmarks, as seen in Figure 2, for a patient with facial palsy fit accordingly for both sides of the face. As patients often have unilateral palsy, only one side of the face is affected, and we view both face sides independently of each other. Thus we assume that neither the healthy nor palsy side introduces a bias to the landmark estimation for the other side. Our fixed camera locations are: *yaw* angles of -40, -20, 20, and 40 degrees and *pitch* angles of -30 and 30 degrees. The pre-trained model uses the virtual cameras RGB and depth images as input [18]. Additionally, we remove rendering pipeline overhead, reduce unnecessary memory access and cache misses, and use new CUDA features. We greatly reduce the computation time for a single surface scan to one second, thus, reducing the processing time for a six-second video to 180 seconds.

4.2   Radial Curves

In a set $\mathcal{X} \in \mathbb{R}^{k \times 3}$ with k points, either a point cloud or the vertices of a mesh, radial curves are a structured description of the scanned surface [2–4, 24]. Radial curves, emitting from a common start point and limited by a maximal distance r, are surface descriptors defined by a tensor $\Gamma \in \mathbb{R}^{n \times m \times 3}$ with n curves with m curve points. In the case of faces, the nose tip is the start point, and the chin limits the distance [2, 4, 24], as depicted in Figure 2. To extract the curve group Γ alignment is crucial, thus, we normalize $\mathcal{X}$ with $\bar{\mathcal{X}} = (\mathcal{X} - T) \cdot R_H^{-1}$. The translation vector $T \in \mathbb{R}^3$ is the nose tip, and $R_H \in \mathbb{R}^{3 \times 3}$ is the head pose obtained from the eye and mouth landmarks [6]. Each radial curve γ_α resides on a plane p_α, defined by normal d_α^n and vector along it d_α, rotated through the

---

[4] All shown individuals agreed to have their images published in terms with the GDPR.

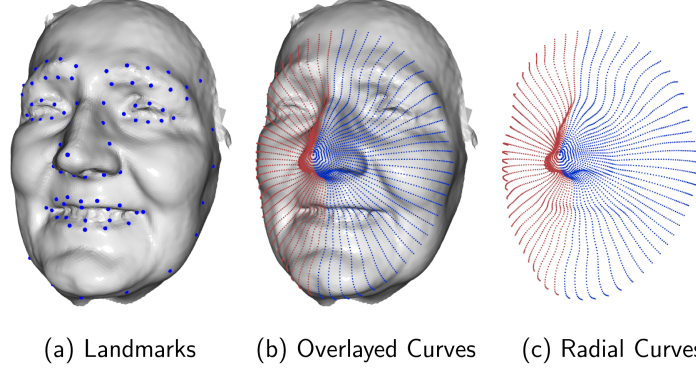(a) Landmarks   (b) Overlayed Curves   (c) Radial Curves

Fig. 2: We highlight the extracted landmarks (a) and the resulting radial curves Γ (b) on the face scan of a patient with facial palsy. In (c), the curves Γ_{left} describe the left (blue) and right Γ_{right} (red) sides of the face.

nose tip with an angle $\alpha = \frac{360°}{n}$. For lateral descriptions, n has to be an even number and greater equals than four [4, 24]. All points in $\bar{\mathcal{X}}$ that lie around the plane p_α with maximal distance δ are selected [4, 24]:

$$S_\alpha = \left\{ x_i \in \bar{\mathcal{X}} \middle| |x_i^T d_\alpha^n| < \delta \wedge x_i^T \cdot d_\alpha > 0 \right\}. \tag{1}$$

With the 3dMD camera system, we use $\delta = 0.8 \; mm$. A temporary projection of S_α onto the plane p_α simplifies ordering and fitting, as seen in Figure 3a. We sort the points by distance to the nose tip [24] and afterward for a correct surface description with a graph traversal algorithm [4]. A 2D spline approximates the curve γ_α in the ordered points $\bar{S}_\alpha$. We equidistantly sample m point between the nose tip and the most distant point, shown in Figure 3d. Lastly, we project the spline points back into the original 3D coordinate system. After computing all n curves, we obtain Γ. Aligning the curve tensor to the scan is only necessary for visualization and is done with $\Gamma := \Gamma \cdot R_H + T$, as seen in Figure 2.

4.3   Lateral Face Mesh Generation

The tensor Γ represents a structured face surface. The pointwise difference between the lateral curve pairs (γ_α and $\gamma_{360-\alpha}$) computes asymmetry [4]. However, this approach neglects the overall state of each face, especially volume information, which is measurable even for small movements [21]. We overcome this limitation by estimating unilateral facial volume based on a watertight mesh of Γ. A watertight mesh is a 2-manifold mesh [7], where every edge is part of precisely two faces [8]. Despite receiving a mesh surface, we create a new volumetric mesh to ensure watertight properties and support point cloud scanners. As we already have a face surface descriptor Γ, we do need general surface reconstruction algorithms [1, 10]. The left tensor Γ_{left} includes all curves γ_α with $\alpha \in [0, 180]$ and

(a) δ area   (b) S_α (c) $\bar{S}_\alpha$ (d) γ_α (e) $\varGamma_{\text{right}}$ (f) Scheme   (g) $\mathcal{M}_{\text{right}}$
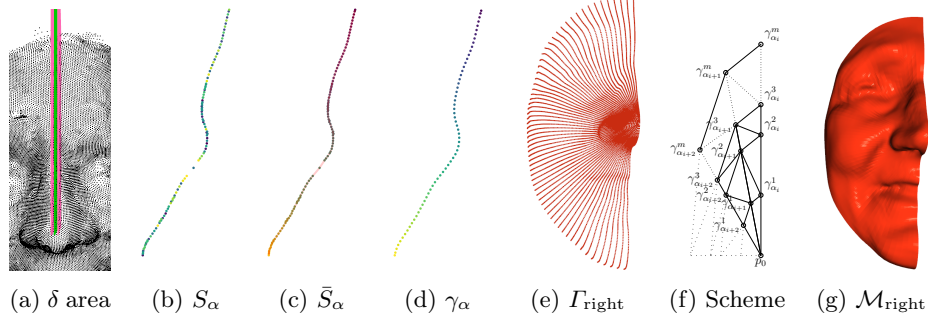
Fig. 3: We visualize each curve extraction process step and the resulting triangulation $\mathcal{M}_{\text{left}}$ of the left facial surface scan. The color coding of S_α, $\bar{S}_\alpha$, and the γ_α indicate the order of the points.

the right tensor $\varGamma_{\text{right}}$ all curves γ_α with $\alpha \in [180, 360]$. Please note, that curve γ_0 and γ_{360} are identical and the views are from the patient's point of view.

$\varGamma_{\text{left}}$ and $\varGamma_{\text{right}}$ construct the closed lateral face surfaces $\mathcal{M}_{\text{left}}$ and $\mathcal{M}_{\text{right}}$, as seen in Figure 3g. The borders of $\mathcal{M}_{\text{left}}$ and $\mathcal{M}_{\text{right}}$ are connected with an underlying sphere mesh, as seen in Figure 4b, and a side mesh along the vertical face center, as seen in Figure 4c. All steps are watertight, and we apply the combined mesh for the volume approximations. A tetrahedron volume can be computed using each triangle, with the origin as the fourth point. We obtain a correct volume by ensuring that the triangle winding order is counter-clockwise [8].

Radial Curve Mesh Generation The generation algorithm is based on the radial curves tensor $\varGamma_{\text{left}}$ and $\varGamma_{\text{right}}$, see Figure 3e. As each curve γ lies on the scan surface of the face, the generated also mesh represents the face surface, see Figure 3g. The degree of detail is adjustable by the number of points m and the number of curves n. Each curve starts at the same point p_0, which is the nose tip of the face. The equidistantly sampled points ensure that points between adjacent curves describe similar perimeter locations. Between two adjacent curves γ_{α_i} and $\gamma_{\alpha_{i+1}}$, we create a triangulation pattern shown in Figure 3f. The triangulation $\mathcal{M}$ includes all points, and the mesh is without holes and watertight. Our approach relies only on the extracted radial curve tensors $\varGamma_{\text{left}}$ and $\varGamma_{\text{right}}$ without any hyperparameters The outer edges of $\mathcal{M}_{\text{left}}$ and $\mathcal{M}_{\text{right}}$ connect to the underlying sphere and side meshes, linking every edge precisely to two faces.

Underlying Sphere Mesh Several approaches are possible to close the volume below the face mesh to enable volume calculations. First, we require a south pole point S as a reference point. We use the endpoint $E1$ of the curve γ_{180} and the endpoint $E2$ of the curve γ_0 as orientation. Additionally, we use the nose tip C as a third reference point, shown in Figure 4a. S is the perpendicular intersection of the centerline and the line connecting $E1$ and $E2$ with the distance r, the

(a) Construction of the arc segments   (b) Triangulated underlying sphere mesh   (c) Mesh using constrained Delaunay triangulation
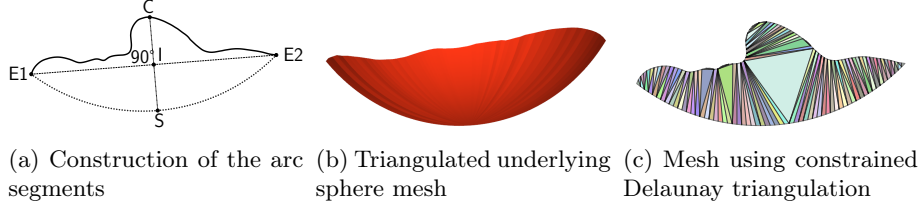
Fig. 4: The side mesh (b) fills the gap between the facial and underlying sphere mesh (a). The inner edges of the radial curves (a) serve as orientation.

same value as for the radial curve extraction, to C. The case of $E1$, $E2$, and C being co-linear cannot occur since these points reference anatomical facial structures and would otherwise indicate a severe facial deformity or a severe error during previous extraction steps. We could use the south pole point S and the boundary points of the face to form simple triangles. However, different facial shapes (e.g., a deep eye socket or mouth being open) will lead to self-intersections [8]. A spherical approach prevents trivial self-intersections, even though theoretically possible but unlikely in practice, as the sphere is convex, and the head will fit inside the sphere. For each radial curve γ_α, we calculate the arc on the corresponding sphere using the corresponding endpoint and S, ensuring alignment with the outer edges of the surface mesh. We triangulate sphere segments like the facial mesh, as depicted in Figure 4b. Consequently, the underlying sphere is closed and directly connected to the scan surface mesh.

Face Side Mesh The final component is the face side closing the facial and sphere mesh gap. A triangulation scheme as in Figure 3f is not feasible due to the different point densities. However, we can use a constrained Delaunay triangulation to fill the gap [5, 17]. We use the curves γ_0 and γ_{180} of the curve tensor Γ and sphere meshes boundary edges to constrain the triangulation, as depicted in Figure 4a. The face side mesh is useable for both the left and right sides of the face. This operation guarantees a watertight mesh, as the boundary edges constrain the triangulation. Therefore, we obtain three watertight meshes, the facial mesh $\mathcal{M}_{\text{left}}$ and $\mathcal{M}_{\text{right}}$, the underlying sphere- and the face side mesh.

4.4 Volume Estimation for Lateral Face Sides

We create a 2-manifold mesh from the radial curve tensor Γ_{left} and Γ_{right}, as described in subsection 4.3. Please note that self-intersections are possible but unlikely in practice. The meshes are watertight and closed, allowing us to estimate the patient's lateral face volume; examples are shown in Figure 6. Summing up the signed tetrahedrons' volumes yields the total volume of the mesh [8]:

$$V = \sum_{i=1}^{n} \frac{1}{6} \cdot (p_i^{(1)} \times p_i^{(2)} \cdot p_i^{(3)}), \tag{2}$$
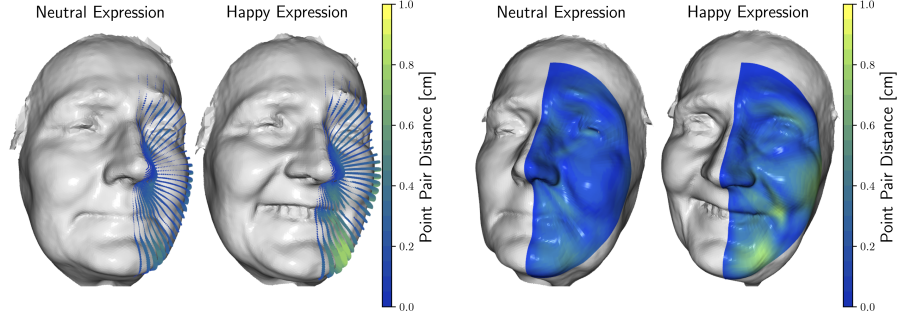
(a) Vector field visualization $\mathcal{V}$ between tensors Γ_{left} and $\bar{\Gamma}_{\text{left}}$.

(b) Projection of the volumetric difference onto the facial surface

Fig. 5: Both visualizations show the disparities (maximum 1 cm) between the left and right sides of the face between the *neutral* and *happy* expressions.

where $p_i^{(1)}$, $p_i^{(2)}$ and $p_i^{(3)}$ are the vertices of the triangle i. We assume all tetrahedrons share the same origin $[0, 0, 0]^T$ as a fourth point. Overlapping tetrahedron bodies cancel each other out due to the triangle's counter-clockwise winding order, thus providing a correct volume estimation. As before, the degree of detail is adjustable by the number of points m and the number of curves n. We observed that the relative difference among the face sides is not affected significantly. We chose $n = 64$ curves and $m = 64$ spline points in our analysis to balance accuracy and computation time. The calculations are conducted in the original coordinate system, resulting in real-world values measured in millimeters.

4.5   Volumetric Difference Visualization

Volume estimation provides crucial information about the disparities between the left and right sides of the face. Additionally, identifying the specific locations of volumetric differences can aid doctors in optimizing the treatment of facial palsy patients. We assume the left side is the palsy side, and the right is the healthy side. Mirroring the curve tensor Γ_{right} along the vertical centerline, defined by γ_0 and γ_{180}, yields $\bar{\Gamma}_{\text{left}}$, which describes the left side without palsy. As the curve tensors and face scan align, we can directly compare the points of Γ_{left} and $\bar{\Gamma}_{\text{left}}$. Due to the equidistant spline sampling, this pointwise correspondence enables us to indicate where the palsy and contralateral sides differ.

For a 3D visualization, we create a vector field $\mathcal{V}$ between pairwise points from Γ_{left} to $\bar{\Gamma}_{\text{left}}$. The vector length measures the side disparities. As the radial curves γ_α lie on the face's surface, the vectors also originate on the surface. For the visualization, we use a sequential colormap (Imola) without dark shades to reduce interference with shadows introduced by the render engine, as depicted in Figure 5a. We set the upper limit of the color range to 1 cm to ensure comparable visualizations between the different time steps. This visualization aids doctors in identifying the affected areas of the palsy side.

Additionally, we project the volumetric differences onto the facial surface, see Figure 5b. This visualization is more intuitive for doctors, who can more easily identify the affected areas without interpreting a vector field or interacting with the 3D renderer. We use the identical color mapping used for the vector field visualization. The projection requires computing the intersection between $\mathcal{V}$ and the facial surface mesh $\mathcal{M}_{\text{left}}$. The vertex colors are then assigned to the corresponding vector length color range value. This approach is similar to [25], indicating the differences between time steps but does not require registration of the facial surface meshes. For example, Figure 5b shows that the chin area is affected more than the cheek area.

5   Volume Analysis during Dynamic Movements

Lastly, we are interested in the dynamic analysis of the facial volume during an instructed movement. Thus, we analyzed patients' volumetric changes and locations mimicking facial expressions. During dynamic movements, temporal noise might occur from the 3dMD camera system (3dMD LCC, Georgia, USA), which propagates to the 3D landmarks and radial curves. Thus, we apply a sliding window of 5 frames to the 3D landmarks to reduce the impact on subsequent processing steps. The radial curve range is set to $r = 85\ mm$, the distance between the nose tip and the chin. Patients were instructed to mimic a *happy* facial expression following a *neutral* phase that lasted about three seconds. We visualize the time progression in Figure 6. The top row displays four face scans, the lateral meshes, and the projected volumetric differences of a patient during selected time steps. The second row illustrates the volume of the left (blue) and right (red) sides of the face, as well as the absolute volume difference between the two sides (black). The third row shows the averaged one-to-one pointwise distance of $\mathcal{V}$ between the affected and contralateral sides [4].

The initial difference might be due to inherent facial asymmetries, muscle atrophy or compensatory hypertrophy, a mixture of both, or inaccuracy in the method. However, as it remains constant during the neutral phase, we assume our method is stable throughout dynamic movements. During the movement phase, the volume difference increases, indicating increasing facial asymmetry for both measurement methods. However, the volumetric analysis enables insight into the impact of both faces sides. The palsy side mesh (left/blue) decreases in volume, whereas the healthy side (right/red) experiences an increase in volume. A change is expected as the facial muscles contract [21]. The volume reduction on the palsy side could be due to tissue pulled towards the healthy side. The facial muscles of both sides form a more extensive interwoven network. Suppose one side (the healthy contralateral side) is contracting stronger. In that case, this automatically pulls over the facial soft tissue (that we observe as volume change) from the palsy side to the healthy side, as the contraction on the healthy side is not counterbalanced by a symmetric activity on the palsy side. Our method exhibits similar behavior to the pointwise distance [4], indicating that it measures the same asymmetry. However, pointwise distance cannot reveal the palsy side's im-
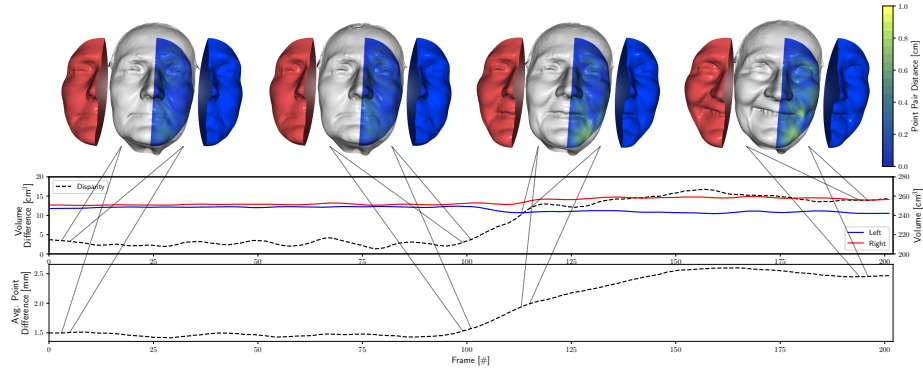
Fig. 6: We measure the volumetric changes from a `neutral` to a `happy` facial expression. The palsy side (blue) decreases while the healthy side (red) increases in volume, indicating a shift from the palsy side to the healthy side.

pact on the healthy side, making volumetric analysis more suitable for assessing this effect. Based on pointwise disparities, our proposed visualization effectively illustrates the volumetric differences between the healthy and palsy sides.

6 Conclusions and Future Work

We introduced a method for calculating volumetric facial disparities, improving on existing approaches and providing insights into the palsy side's impact. In addition, our approach also offers visualization of volumetric differences, enhancing facial asymmetry understanding. Moreover, we can analyze dynamic changes during a single movement, extending the method's usefulness.

As our approach is automatic and requires minimal parameter tuning (number of radial curves n, spline points m, and δ based on the sensor), we do not rely on any assumptions and estimations about facial symmetry. The joint visualization, see Figure 6, of the volume differences, the facial expression, and the difference heatmap helps to understand the behavior of the facial muscles during a single movement. The projected volumetric differences between the meshes, see Figure 5b, can be used to identify the affected areas of the face in a single image. Visualizations guide treatment decisions during the clinical routine, and our approach can help doctors better understand facial asymmetry. This insight is significant for treating facial palsy, as the muscle contractions create facial expressions. Our work offers a combined tool to analyze facial volume changes during dynamic movements bridging the gap between static and dynamic analysis based on 3D data. We open up future medical research to define instance exercises that address counter-actions to volume shifts towards the healthy side.

Our approach's effectiveness depends on 3D scan quality and intermediate facial landmark estimation. Our future work aims to join 3D morphable models with radial curves, enabling the automatic identification of affected facial regions.

References

1. Bernardini, F., Mittleman, J., Rushmeier, H., Silva, C., Taubin, G.: The ball-pivoting algorithm for surface reconstruction. IEEE Transactions on Visualization and Computer Graphics **5**(4), 349–359 (Oct 1999). https://doi.org/10.1109/2945.817351

2. Berretti, S., Del Bimbo, A., Pala, P., Mata, F.J.S.: Face recognition by SVMS classification of 2D and 3D Radial Geodesics. In: 2008 IEEE International Conference on Multimedia and Expo. pp. 93–96. IEEE, Hannover, Germany (Jun 2008). https://doi.org/10.1109/ICME.2008.4607379

3. Bowman, A.W., Katina, S., Smith, J., Brown, D.: Anatomical curve identification. Computational statistics & data analysis **86**, 52–64 (2015). https://doi.org/10.1016/j.csda.2014.12.007

4. Büchner, T., Sickert, S., Volk, G.F., Guntinas-Lichius, O., Denzler, J.: Automatic Objective Severity Grading of Peripheral Facial Palsy Using 3D Radial Curves Extracted from Point Clouds. Challenges of Trustable AI and Added-Value on Health pp. 179–183 (2022). https://doi.org/10.3233/SHTI220433

5. Delaunay, B.N.: Sur la sphère vide. Bulletin de l'Académie des Sciences de l'URSS. VII. Série **1934**(6), 793–800 (1934)

6. Derkach, D., Ruiz, A., Sukno, F.M.: Head pose estimation based on 3-D facial landmarks localization and regression. In: 2017 12th IEEE International Conference on Automatic Face & Gesture Recognition (FG 2017). pp. 820–827. IEEE (2017)

7. Edelsbrunner, H.: Surface Reconstruction by Wrapping Finite Sets in Space. In: Aronov, B., Basu, S., Pach, J., Sharir, M. (eds.) Discrete and Computational Geometry: The Goodman-Pollack Festschrift, pp. 379–404. Algorithms and Combinatorics, Springer, Berlin, Heidelberg (2003). https://doi.org/10.1007/978-3-642-55566-4_17

8. Giblin, P.: Graphs, Surfaces and Homology. Cambridge University Press, Cambridge, 3 edn. (2010). https://doi.org/10.1017/CBO9780511779534

9. Haase, D., Minnigerode, L., Volk, G.F., Denzler, J., Guntinas-Lichius, O.: Automated and objective action coding of facial expressions in patients with acute facial palsy. European Archives of Oto-Rhino-Laryngology **272**(5), 1259–1267 (May 2015). https://doi.org/10.1007/s00405-014-3385-8

10. Kazhdan, M., Bolitho, M., Hoppe, H.: Poisson Surface Reconstruction. The Eurographics Association (2006). https://doi.org/10.2312/SGP/SGP06/061-070

11. Li, T., Bolkart, T., Black, M.J., Li, H., Romero, J.: Learning a model of facial shape and expression from 4D scans. ACM Transactions on Graphics **36**(6), 1–17 (Nov 2017). https://doi.org/10.1145/3130800.3130813

12. Lou, J., Yu, H., Wang, F.Y.: A Review on Automated Facial Nerve Function Assessment From Visual Face Capture. IEEE Transactions on Neural Systems and Rehabilitation Engineering **28**(2), 488–497 (Feb 2020). https://doi.org/10.1109/TNSRE.2019.2961244

13. Lugaresi, C., Tang, J., Nash, H., McClanahan, C., Uboweja, E., Hays, M., Zhang, F., Chang, C.L., Yong, M.G., Lee, J., Chang, W.T., Hua, W., Georg, M., Grundmann, M.: MediaPipe: A Framework for Building Perception Pipelines (Jun 2019). https://doi.org/10.48550/arXiv.1906.08172

14. Miller, M.Q., Hadlock, T.A., Fortier, E., Guarin, D.L.: The Auto-eFACE: Machine Learning-Enhanced Program Yields Automated Facial Palsy Assessment Tool. Plastic and Reconstructive Surgery **147**(2), 467–474 (Feb 2021). https://doi.org/10.1097/PRS.0000000000007572

15. Özsoy, U., Sekerci, R., Hizay, A., Yildirim, Y., Uysal, H.: Assessment of reproducibility and reliability of facial expressions using 3D handheld scanner. Journal of Cranio-Maxillo-Facial Surgery: Official Publication of the European Association for Cranio-Maxillo-Facial Surgery **47**(6), 895–901 (Jun 2019). https://doi.org/10.1016/j.jcms.2019.03.022

16. Patel, A., Islam, S.M.S., Murray, K., Goonewardene, M.S.: Facial asymmetry assessment in adults using three-dimensional surface imaging. Progress in Orthodontics **16**(1), 36 (Oct 2015). https://doi.org/10.1186/s40510-015-0106-9

17. Paul Chew, L.: Constrained delaunay triangulations. Algorithmica **4**(1), 97–108 (Jun 1989). https://doi.org/10.1007/BF01553881

18. Paulsen, R.R., Juhl, K.A., Haspang, T.M., Hansen, T., Ganz, M., Einarsson, G.: Multi-view consensus CNN for 3D facial landmark placement. arXiv:1910.06007 [cs] **11361**, 706–719 (2019). https://doi.org/10.1007/978-3-030-20887-5_44

19. Paysan, P., Knothe, R., Amberg, B., Romdhani, S., Vetter, T.: A 3D Face Model for Pose and Illumination Invariant Face Recognition. In: 2009 Sixth IEEE International Conference on Advanced Video and Signal Based Surveillance. pp. 296–301. IEEE, Genova, Italy (Sep 2009). https://doi.org/10.1109/AVSS.2009.58

20. Raj, A., Mothes, O., Sickert, S., Volk, G.F., Guntinas-Lichius, O., Denzler, J.: Automatic and Objective Facial Palsy Grading Index Prediction Using Deep Feature Regression. In: Papież, B.W., Namburete, A.I.L., Yaqub, M., Noble, J.A. (eds.) Medical Image Understanding and Analysis, vol. 1248, pp. 253–266. Springer International Publishing, Cham (2020). https://doi.org/10.1007/978-3-030-52791-4_20

21. Rawlani, R., Qureshi, H., Rawlani, V., Turin, S.Y., Mustoe, T.A.: Volumetric Changes of the Mid and Lower Face with Animation and the Standardization of Three-Dimensional Facial Imaging. Plastic and Reconstructive Surgery **143**(1), 76–85 (Jan 2019). https://doi.org/10.1097/PRS.0000000000005082

22. Sarhan, F.R., Olivetto, M., Ben Mansour, K., Neiva, C., Colin, E., Choteau, B., Marie, J.P., Testelin, S., Marin, F., Dakpé, S.: Quantified analysis of facial movement: A reference for clinical applications. Clinical Anatomy p. ca.23999 (Jan 2023). https://doi.org/10.1002/ca.23999

23. ten Harkel, T.C., Vinayahalingam, S., Ingels, K.J.A.O., Bergé, S.J., Maal, T.J.J., Speksnijder, C.M.: Reliability and Agreement of 3D Anthropometric Measurements in Facial Palsy Patients Using a Low-Cost 4D Imaging System. IEEE Transactions on Neural Systems and Rehabilitation Engineering **28**(8), 1817–1824 (Aug 2020). https://doi.org/10.1109/TNSRE.2020.3007532

24. Thümmel, M., Sickert, S., Denzler, J.: Facial Behavior Analysis using 4D Curvature Statistics for Presentation Attack Detection. In: 2021 IEEE International Workshop on Biometrics and Forensics (IWBF). pp. 1–6 (May 2021). https://doi.org/10.1109/IWBF50991.2021.9465080

25. Volk, G.F., Thümmel, M., Mothes, O., Arnold, D., Thielker, J., Denzler, J., Mastryukova, V., Mayr, W., Guntinas-Lichius, O.: Long-term home-based Surface Electrostimulation is useful to prevent atrophy in denervated Facial Muscles. In: Vienna Workshop on Functional Electrical Stimulation (FESWS) (2019)

26. Zhuang, Y., McDonald, M.M., Aldridge, C.M., Hassan, M.A., Uribe, O., Arteaga, D., Southerland, A.M., Rohde, G.K.: Video-Based Facial Weakness Analysis. IEEE transactions on bio-medical engineering **68**(9), 2698–2705 (Sep 2021). https://doi.org/10.1109/TBME.2021.3049739